Final Technical Report – Award # G18AP00022

Title of Award: Roles of Stress Heterogeneity and Stress Interaction in Induced Seismicity: Example from the Fairview/Woodward Area in Oklahoma

Principle Investigators & Authors: Xiaowei Chen[1] and Jacob Walter[2]

Main participants: Xiaowei Chen, Yan Qin, Jacob Walter, Qimin Wu

1. School of Geosciences, the University of Oklahoma, Norman, OK, 73019
        Phone: (405)-325-3253
2. Oklahoma Geological Survey, the University of Oklahoma, Norman, OK, 73019
        Phone: 405-325-8497

Author emails: xiaowei.chen@ou.edu; jwalter@ou.edu

Term covered by the award: 05/2018 – 05/2020

Table of Contents

Abstract:

Oklahoma has experienced significant seismicity rate increase in the past decade. While it is well established that most of the increased seismicity is due to wastewater disposal, and the triggering mechanism is generally understood as pressure triggering critically stressed faults for a given regional stress field, some areas in Oklahoma exhibit substantial complexity, and some unfavorably oriented faults are reactivated. In this project, we first examined detailed stress field in Oklahoma and south Kansas with over 4000 focal mechanism solutions, and the stress state of seismogenic faults and geological faults. These results are published in Qin et al., (2019). Then we focus on selected sequences to investigate detailed spatiotemporal evolutions of stress state within individual fault zones. We started with a well-recorded sequence in central Oklahoma to test the analysis method, and obtained detailed source complexity of a Mw4 earthquake (Wu et al., 2019). We move on the detailed focal mechanism solutions and stress state evolutions for smaller earthquakes with both a cross-correlation based polarity picking method and a machine learning method. The results show substantial differences in the percentage of optimally oriented events for two sequences with M5 earthquakes and two sequences with maximum magnitude ≤4 that are more swarm-like, suggesting that pre-existing geological structure influences maximum magnitude and temporal evolution of sequences. Finally, we apply a matched-filter based detection to Woodward and Fairview area to better understand the temporal evolutions of the sequences. The new catalog showed that these two sequences started much earlier than recorded by the catalog.

Report:

1. Introduction

The project was motivated by the observation in western Oklahoma on the Woodward and Fairview sequences. The two faults are located within 20 km of each other, but have very different fault orientations (rotated by 20 degrees). If the stress field and friction are both homogeneous, then both faults cannot be both optimally oriented. The two faults appear to have similar fault length from catalog earthquake locations, but the Woodward fault does not have any M4+ earthquakes, while the Fairview fault has 9 M4+ earthquakes and a maximum magnitude of 5. These different faulting behaviors and complex temporal evolutions of seismicity make the Fairview/Woodward area an ideal case to probe the roles of stress heterogeneity and stress interactions in induced earthquake sequences.

However, the two areas are located near the western edge of the Oklahoma network coverage, even with enhanced coverage after the M5 Fairview earthquake, the Woodward sequence still have limited azimuthal coverage. So, we started with an overview of Oklahoma and south Kansas using cataloged focal mechanism solutions to better understand stress state distributions for all mapped seismogenic faults and geological faults. Then, we tested the algorithms for source time function and focal mechanism inversion using a well-recorded sequence in central Oklahoma. Finally, we apply the algorithms that are tested and validated using well-recorded earthquakes to Woodward and Fairview areas.

In this report, we combine these studies conducted during the term covered by the USGS award to investigate the complexities in earthquake sources, stress field and stress states for wastewater induced earthquakes in the Oklahoma. Two studies are published: Qin et al., (2019) and Wu et al.,

(2019), two more are being prepared for publication. The report will contain summaries of each study and an overall conclusion based on all studies.

2. Overview of stress state of seismogenic faults

The first step is to obtain a high resolution stress map, and an overview of stress states of seismogenic faults. With these results, we expect to address the following questions: (1) are there stress heterogeneities in stress field? (2) are all faults reactivated optimally oriented? (3) how does pore pressure influence stress field and fault activations? Included in the report is a short summary of key methods and results from Qin et al., (2019), for more details, please refer to the published study.

2.1 Method

2.1.1 Mapping seismogenic faults

We use a hierarchical clustering program in MATLAB to cluster the earthquakes based on the epicenter of the relocations from relocated catalogs *(Chen, 2016; Schoenball & Ellsworth, 2017)* . In this method, the events are linked based on the nearest distance between each event pair, and a distance cutoff of 0.46 km is selected by trial and error to group events with distance smaller than the cutoff into a cluster. The program identifies 84 clusters with more than 30 events (Figure 1). We use a relatively longer distance cutoff in the clustering process, and some clusters include several trends of events close to each other, which are then separated manually to calculate the fault geometries. For each cluster and some manually separated subclusters with 30 or more events, we use principal component analysis to fit a fault plane *(Vidale & Shearer, 2006)* and obtain the strike/dip of each fault.
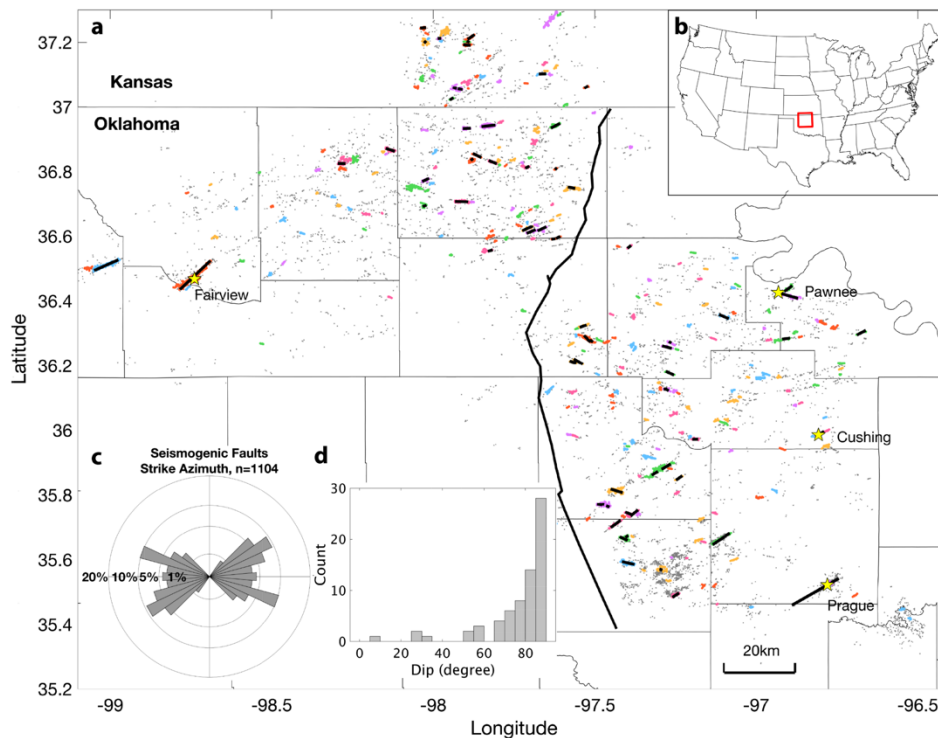

Figure 1. Mapped faults in this study based on earthquake relocations from Chen (2016) and Schoenball and Ellsworth (2017). (a) Earthquake clusters (colored dots) with 10 and more events. Short, black lines show the faults with planarity larger than 0.8 mapped from 30 and more events. Yellow stars show the location of four $M \geqslant 5$ earthquakes in Oklahoma. Thin, black lines are county boundaries in Oklahoma. The long, thick black line is the Nemaha fault from OGS fault database (Marsh & Holland, 2016). (b) The inset map shows the location of the study area. (c) Histogram of strike of faults in (a). (d) Histogram of dip of faults in (a).

2.1.2 Stress inversion

To obtain a detailed in situ stress field, we use the MSATSI software package *(Martínez-garzón et al., 2014)* to invert the stress field from earthquake focal mechanism solutions. The MSATSI software is a MATLAB wrapper of the SATSI *(Hardebeck & Michael, 2006)* based on the inversion from *(Michael, 1984)*. With 2,047 focal mechanism solutions for Oklahoma and southern Kansas, the study area is first gridded with 0.4° by 0.4°, and if 100 or more events are in one grid, the grid is then subdivided into two or four evenly spaced subgrids in latitude and longitude as long as there are still more than 50 events in each subgrid. As a result, the study area is sepa- rated into 24 grids, and a damped inversion is performed on those grids. The inversion results include the orientations of the three principal stress axes and a measure of their relative amplitudes R:

$$R = \frac{\sigma_1 - \sigma_2}{\sigma_1 - \sigma_3}, \tag{1}$$

where σ_1, σ_2, and σ_3 are the maximum, intermediate, and minimum principal stresses, respectively. The uncertainties of the inversion results are estimated by 1,000 bootstrap resamplings of the focal mechanism solutions associated within each grid.

2.1.3 Focal mechanism tomography and stress state

The focal mechanism tomography (FMT) technique was developed to estimate the fluid pore pressure field from earthquake focal mechanism solutions under a given stress field *(Terakawa et al., 2010)*. In this study, we adopt the assumptions in *Terakawa et al. (2010)* to convert the relative stress amplitude to a 3-D stress tensor and use the local stress tensor to evaluate the stress state of individual faults. We compare results with local stress tensor and averaged stress tensor. With the stress tensor known, we compute shear and normal stress on faults, project them onto Mohr circle, and calculate the required pore pressure for fault failure. To project all faults onto the same 3-D Mohr circle, we keep the local stress orientations of each grid and calculate a uniform stress amplitude by averaging over all grids. The stress amplitudes and fluid pore pressure calculated from the above assumptions are proportional to the depth. As the catalogs we use have relatively large depth uncertainty, the depth of the mapped faults is not well resolved. We introduce a normalized parameter *understress* to eliminate the depth dependence of the fault stress state following *Gischig, (2015)*:

$$understress = (\tau_p - \tau_0)/\tau_p, \tag{2}$$

where τ_0 is shear stress on the fault calculated from the fault geometry and stress orientations and τ_p is shear stress at which slip initiates based on the Coulomb failure criterion under hydrostatic pore pressure. Since both τ_0 and τ_p increase linearly with depth, the defined parameter *understress* is independent of depth. The *understress* can be used to quantitatively measure fault criticality relative to local stress field. Values of *understress* near 0 imply that the faults are critically stressed, while values near 1 imply negligible resolved shear stress applied on the fault, and the fault is least favorably oriented. We also calculate the parameter of excess pore pressure, which is defined as the required pore pressure increase above hydrostatic pressure for fault failure according to Mohr circle.

2.3 Result and Discussions

2.3.1 Stress field and fluid pressure

Stress inversion provides a stress field with higher spatial resolution compared to previous studies in Oklahoma. Figure 2 shows the map view of maximum horizontal compressive stress (σ_{Hmax}) orientations colored by faulting type. Central Oklahoma is mostly in a strike-slip faulting regime

(green bars), whereas north and northwest Oklahoma show a transition from strike-slip to oblique normal faulting regime (black bars). The dominant orientation of σ_{Hmax} is 80–90∘ (Figure 2b). Those observations are consistent with previous studies (e.g., *Alt & Zoback, 2017*). The stress field in southern Kansas is characterized by strike-slip faulting with σ_{Hmax} of 75–82∘, which are consistent with *Rubinstein et al., (2018)*.
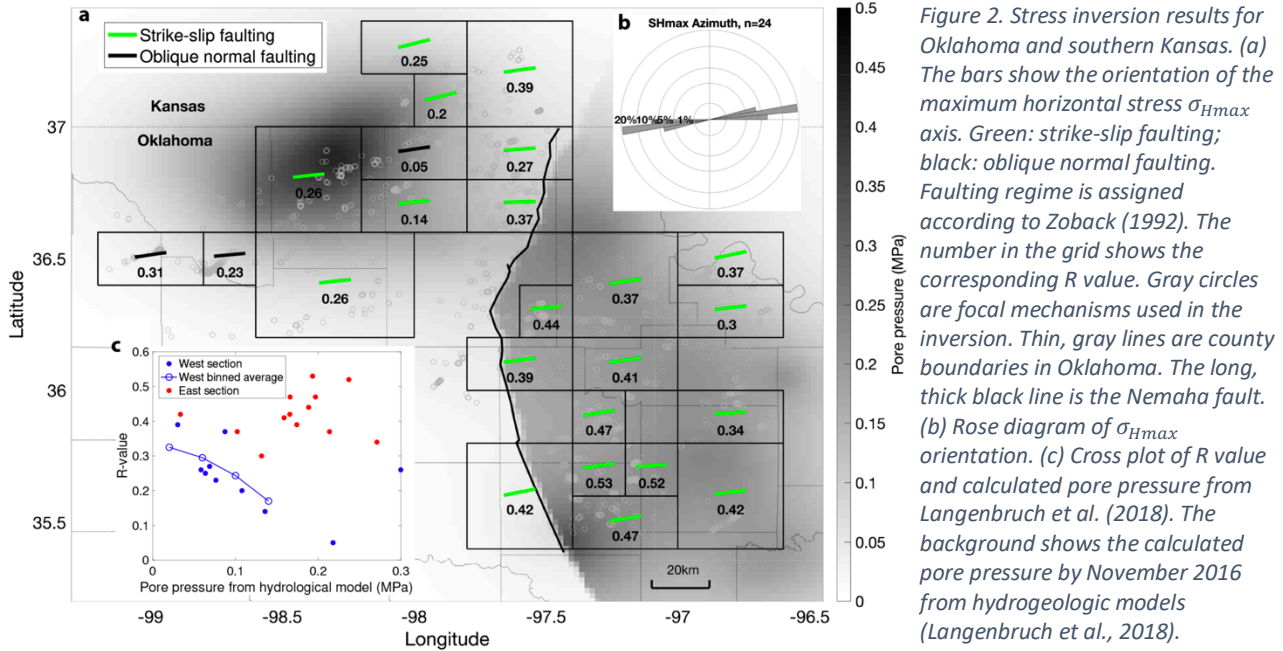

Figure 2. Stress inversion results for Oklahoma and southern Kansas. (a) The bars show the orientation of the maximum horizontal stress σ_{Hmax} axis. Green: strike-slip faulting; black: oblique normal faulting. Faulting regime is assigned according to Zoback (1992). The number in the grid shows the corresponding R value. Gray circles are focal mechanisms used in the inversion. Thin, gray lines are county boundaries in Oklahoma. The long, thick black line is the Nemaha fault. (b) Rose diagram of σ_{Hmax} orientation. (c) Cross plot of R value and calculated pore pressure from Langenbruch et al. (2018). The background shows the calculated pore pressure by November 2016 from hydrogeologic models (Langenbruch et al., 2018).

The stress amplitude ratio R also shows spatial variations. The stress field in northern Oklahoma and south- ern Kansas show smaller R values than other areas, which might indicate the influence of pore pressure. The study area is separated into two major pressure zones using the Nemaha fault as a pressure boundary, referred to as the eastern and western pressure zones *(Haffener et al., 2018)*.

To further understand the influence of pore pressure on stress field, we obtain the pore pressure for each grid by averaging pressure values from *Langenbruch et al., (2018)* at the median occurrence time from all earthquakes within each grid. Using pore pressure values at all grids, we calculate an average R value from all R values within each pressure bin of 0.04 MPa. The result is shown in Figure 2c. For the area west of Nemaha Fault Zone, we obtain negative correlation between R value and pore pressure. However, the eastern Oklahoma region does not show a clear relationship between R value and pore pressure.

The observed negative relationship between R and pore pressure in western pressure zone in Figure 2c could possibly reflect the poroelastic effects by injection. Altmann et al. (2014) gives the analytical solutions to poroelastic equations in 3-D isotropic, homogeneous space.
(Martínez-Garzón et al., 2013) has observed that stress perturbation due to fluid injection decreases over time with repeated injections. The lack of correlation between R and pore pressure in the eastern section is likely due to the overall higher pore pressure from the longer injection period (e.g., *Keranen et al., 2014*).

2.3.2 Fault stress state and reactivation

Using the FMT method, we first calculate the uniform principal stress amplitude gradients as $\sigma_1 = 30.0$ MPa/km, $\sigma_2 = 24.8$ MPa/km, and $\sigma_3 = 15.5$ MPa/km under $\mu = 0.68$. Based on the fault orientation and regional stress field, the shear and normal stress on seismogenic faults are calculated and plotted on 3-D Mohr circle. The understress parameter on each fault is determined by equation (2). As shown in Figure 3, each fault is projected onto a 3-D Mohr circle as a point
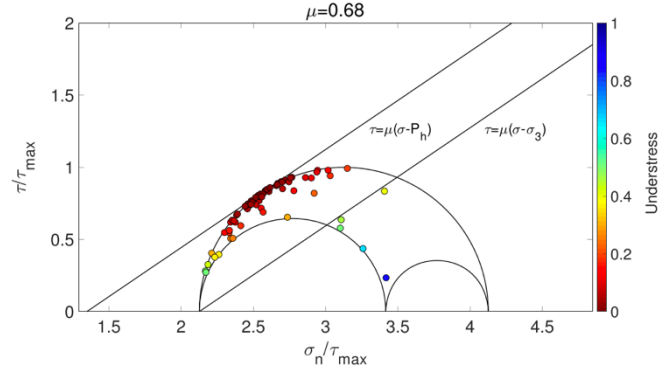

Figure 3. The stress state of 69 seismogenic faults in a 3-D Mohr diagram. The three semicircles represent the stress tensor, and the two straight lines represent the fault strength under hydrostatic fluid pressure and lithostatic pressure under friction coefficient of 0.68. Each circle, colored by understress value, represents the shear and normal stress on a single fault.

colored by its *understress* value. Most faults (78%) are close to failure limit of the hydrostatic fault strength with *understress* smaller than 0.2. Four faults with small dip angle <35◦ show large *understress* (>0.5). This is possibly due to large uncertainties of the dip angle, and the indication of tensile failure (fluid pressure beyond σ_3) is actually an artifact. Other than that, there are still several non-optimally oriented faults being reactivated, which might occur at step overs or rotations at different segments of the optimally oriented fault and result from either high pore pressure increase or other factors, for example, static stress change from earthquakes on the main fault.

The required pore pressure to induce failure on each fault is calculated from FMT and shown in Figure 4. The median and mean excess pore pressure (above hydrostatic pore pressure) is 2.7 and 6.9MPa, respectively under an assumption of fault depth of 5 km. The uniform depth is chosen because the depth of seismogenic faults is not well constrained, and the earthquakes have an average depth of 5 km. The required pore pressure increases are consistent with the estimated pore pressure using similar geomechanical analysis for multiple induced clusters in Texas *(Snee & Zoback, 2016; Quinones et al., 2018)*.

To study the relationship between pore pressure and fault reactivation, we compare our results to the modeled pore pressure from *Langenbruch et al. (2018)*. The modeled pore pressure map is overlain by seismogenic faults colored by excess pore pressure computed in this study in Figure 4. As a qualitative first-order observation, the faults that are misoriented and require a relatively larger pore pressure increase are distributed close to the higher pore pressure areas in central and northern Oklahoma.

2.3.3 Faults with M≥5.0 earthquakes

Since 2011, four large earthquakes (M≥ 5.0) have occurred in Oklahoma: the M5.7 Prague earthquake in 2011, and the M5.1 Fairview, M5.8 Pawnee, and M5.0 Cushing earthquakes in 2016. None of these earth- quakes occurred along previously mapped faults *(Chen et al., 2017; Yeck et al., 2016)*. The geometries of the seismogenic faults delineated from seismicity are mostly consistent with the focal mechanism solutions ofthe mainshocks. With an in situ stress field, we
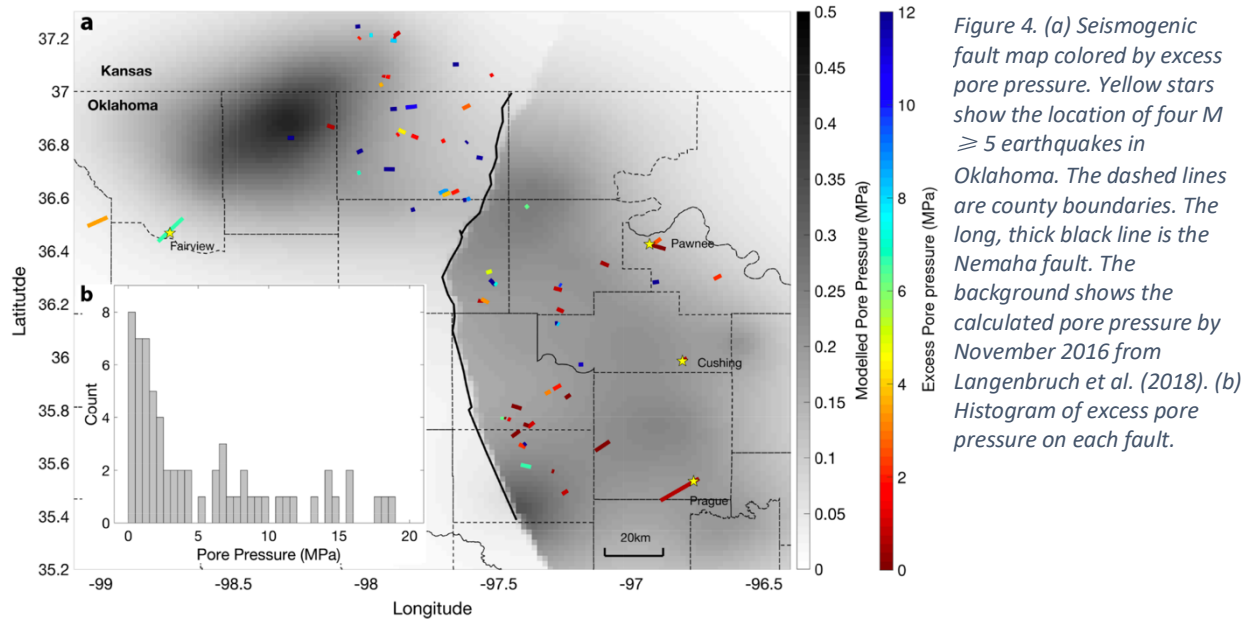
calculate the stress state of the mainshock fault planes from focal mechanism solutions and the corresponding seismogenic faults with the assumption of a constant friction coefficient of $\mu =$ 0.68. As shown in Figure 8, the faults that hosted the M5.7 Prague, M5.8 Pawnee, and M5.0 Cushing earthquakes have *understress* smaller than 0.02, suggesting the faults in Prague, Pawnee, and Cushing were critically stressed and failed under a small perturbation of pore pressure. The seismogenic fault in Fairview is the least optimally oriented with an *understress* parameter of 0.1, and the fault plane of the mainshock has even higher *understress* of 0.2, which is likely due to the shallower dip- ping angle of 66°. *Goebel et al., (2017)* calculated poroelastic stress perturbations in the Fairview area from a group of high-rate injection wells to the northeast. Their results suggest that the poroelastic stress increase at the distance of the Fairview area is about 100 kPa and the fault orientation is about 15° off the optimal orientation that would receive maximum Coulomb stress change. Their results are consistent with the relatively high understress value obtained here for the Fairview fault. Figure 5 also shows that Fairview fault has highest relative shear stress compared to the other three faults, indicating highest frictional strength *(Yoshida et al., 2016)*. The relative frictional strength variations are qualitatively consistent with observations in *Wu et al., (2018)*, where the Fairview fault has highest overall stress drop compared to the other fault zones, similar to the observations for a fluid induced earthquake swarm in Japan *(Yoshida et al., 2017)*.

Gischig, (2015) performed numerical modeling to investigate the effect of the fault orientation on rupture propagation, and the results suggest that optimally oriented faults tend to have uncontrolled ruptures that propagate beyond the pressure front, while less optimally oriented faults tend to have ruptures controlled by the extent of the pressurized zones. From this perspective, the *understress* parameter can provide insight into the fault rupture process, and hence the seismicity distribution for the M5 sequences. To the first order, the Prague, Pawnee, and Cushing sequences, which are on optimally oriented fault planes, are predominantly mainshock-aftershock sequences, with large values of skewness of moment release *(Zhang & Shearer, 2016)*, while the Fairview sequence on the least optimally oriented fault is mainly a swarm-type sequence with an extended foreshock sequence leading up to the M5 earthquake resulting in the smallest skewness. Thus, our findings

are at least consistent with a hypothesis that the fault criticality influences the temporal evolution of earthquake sequences.

Figure 5. Understress for (a) the focal mechanism solutions of M ⩾ 5.0 mainshocks and (b) the hosting seismogenic faults as listed in Table S1. Diamonds: focal mechanism solutions. Circles: seismogenic faults. Both symbols are colored by understress values and scaled with the magnitude of the mainshock. Pr = Prague; Pa = Pawnee; C = Cushing; F=Fairview.
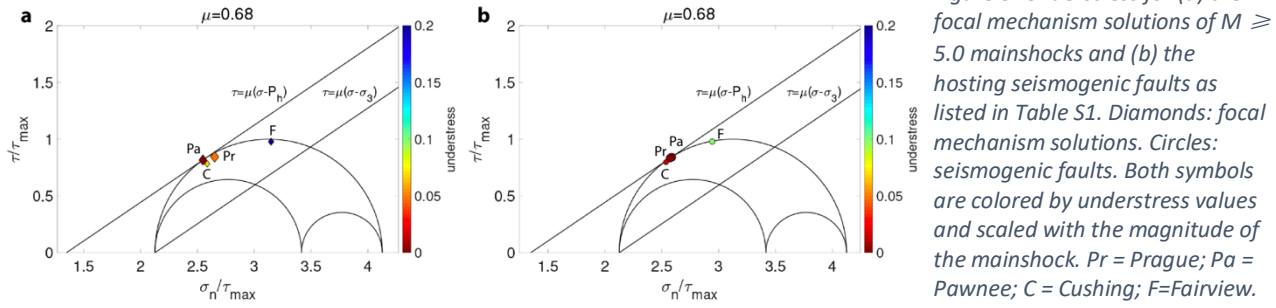
2.4 Summary

In this study, we thoroughly analyzed the stress field at finer spatial scales than previous studies. We find that there exist stress heterogeneities within Oklahoma and southern Kansas, and we observe systematic stress rotations. In western Oklahoma, we observe strong correlation between stress field and pore pressure, suggesting that pore pressure has influenced stress field variations. With improved stress map, we analyzed stress states for seismogenic faults (mapped from relocated earthquakes) and geological faults based on an improved stress map. Analysis of the four faults with M≥5 earthquakes suggests that the Fairview fault is least optimally oriented compared to other M5 earthquakes, which may explain the extended foreshock sequences for the Fairview event compared to other sequences.

3. Complexity within individual faults

The overview study suggested that most seismogenic faults are optimally oriented, however, there do exist less optimally oriented faults. In particular, the Fairview fault is significantly less optimally oriented compared to the other faults that hosted M≥5 earthquakes. This motivated us to examine evolutions of individual sequences. We performed detailed source modeling of a largest event of a swarm sequence (*Wu et al., 2019*), and performed analysis of small earthquake focal mechanism and stress states for four sequences (Qin et al., 2020, in prep).

3.1 The role of earthquake interaction on individual sequences

Prior to the USGS award, we published a study focusing on the Coulomb stress interactions during the Woodward sequence *(Qin et al., 2018)*. In this study, we found sequential activation of the Woodward sequence from Coulomb stress interaction among different fault patches. The Coulomb stress amplitude from earthquakes is comparable to pore pressure or poroelastic stress amplitudes from fluid injection.

Similar observations were made during the Guthrie earthquake sequence in central Oklahoma *(Wu et al., 2019)*. Using Empirical Green's Function (EGF) method, we developed an iterative deconvolution method to obtain the relative source time functions (RSTF) of the Mw4 Guthrie earthquake in central Oklahoma. The RSTF revealed that the Mw4 earthquake had at least four well separated sub-events, indicating strong inter-patch triggering during the rupture process. The

complexity for the Mw4 earthquake is comparable to large interplate earthquakes *(Ye et al., 2018)*. The early aftershocks of the Mw4 earthquake exhibited strong directivity effect, with most early events occurring in the rupture direction (SE direction).

The observations from *Wu et al. (2019)* suggested that complex fault mesh network may cause complexities in earthquake rupture, and that earthquake interaction is an important factor in spatiotemporal evolution of induced earthquake sequences.

3.2 The spatiotemporal evolutions of fault activation

Based on observations from the Woodward and the Guthrie sequences, we hypothesize that small earthquakes during the same sequence have different stress state and occurred along different fault segments. To better understand individual sequence, we need a more complete focal mechanism catalog than *Qin et al., (2019)*. However, picking the polarities for small earthquakes is difficult due to the low signal to noise ratio. Here, we select two methods, waveform-correlation-derived relative polarities *(David R. Shelly et al., 2016)* and a pre-trained deep learning model for polarity classification *(Ross et al., 2018)*. The results from the two methods are then combined to invert moment tensor. With improved moment tensor catalog, we investigate the spatiotemporal evolutions of stress state using the same method as in *Qin et al., (2019)*.

3.2.1 Method

3.2.1.1 SVD method

We follow the method from *Shelly et al., (2016)* to derive P polarities for a whole sequence (N events) based on the M templates with manually picked polarities. The templates are randomly selected. In this method, the waveform cross correlation coefficients are calculated between the N events and M selected templates. For each event-template pair, the weighted relative polarity measurement, which is defined by the absolute difference between the peak and the secondary peak of cross correlations multiplied by the sign of the peak correlation, is used to measure the similarity between the event and template waveform.

The weighted relative polarity measurements form a N by M matrix, which is then represented by the left singular vector of the left unitary matrix of its Singular Value Decomposition (SVD). This vector represents the polarity pattern of all events on a specific station and channel. We measure a consistency factor by comparing the SVD-derived polarities to the manually picked polarities. The consistency factor w_t is defined as,

$$w_t = \frac{\sum w_{cat} \times Pol_{svd}}{\sum(|w_{cat} \times Pol_{svd}|)} \tag{3}$$

where w_{cat} is the manually picked polarity, and Pol_{svd} is the SVD-derived polarity. The SVD-derived P polarities are then multiplied by the consistency factor to get the real polarity for a particular channel.

3.2.1.2 Machine learning method

We adopt the pre-trained convolutional neural network (CNN) model from *Ross et al., (2018)* to pick the polarities. The model was trained by over two million of analyst picked polarities of earthquakes in California. We apply the same preprocessing to the waveform data as in the paper

(Ross et al., 2018). The waveform is resampled to 100 Hz, detrended and filtered between 1 and 20 Hz. Then we select a 4-s-long window centered on P arrival time and normalize the waveform by the peak absolute amplitude in the window. The CNN model takes the 400-point time series as input and predicts the P polarities. The results are measured using precision for each class of polarity (up and down). For a given class, the precision is defined as the number of true positives divided by the total number of records assigned to the class by the CNN model.

$$precison_u = \frac{TP_{uu}}{TP_{uu}+\epsilon_{du}}; precision_d = \frac{TP_{dd}}{TP_{dd}+\epsilon_{ud}} \qquad (4)$$

where u and d represent polarity up and down, TP is the number of true positives, and ϵ is the number of false positives.

According to *Ross et al., (2018)*, the precision rate is influenced by the magnitude of the event, the distance between event and stations, and the SNR of the waveform. We test on the template events in Oklahoma, and the precision rate changes with distance and SNR, not significantly with magnitude, consistent with the findings in California. And the precision rate is comparable to the results *Ross et al., (2018)*. The successful application of the model trained by earthquakes in California to earthquakes in Oklahoma suggests the generalization of the model.

3.2.1.3 Focal mechanism inversion

With the derived polarities from different methods in the previous section, we compute the earthquake focal mechanism solutions in hybridMT *(Kwiatek et al., 2016)*. To ensure the quality of the inversion, we only events with a minimum number of polarities of eight, a maximum azimuthal gap of 120º, and a maximum takeoff angle gap of 60º. We perform the moment tensor inversion with the original data and additional 100-times resampled input dataset by assuming 1% of input phases have wrongly picked polarity based on the precision by comparing the polarities from the two methods above to the cataloged polarity picks.

We use the similar criterion as in HASH program *(Hardebeck & Shearer, 2003)* to assign the quality of the inverted focal mechanisms. The criterion include the probability that the results from resampling are within certain rotation angle (45º) to the preferred solution (PROB), the RMS angular difference between the preferred solution and those from resampling (RMS$_{ANG}$), the fraction of misfit polarities (MFIT) of the preferred solution, and the station distribution (STDR) around the event.

3.2.1.4 Fault stress state

Once we get the focal mechanisms for individual events in each sequence, we follow the statewide analysis in *Qin et al., (2019)* to calculate the fault stress state. The events are projected onto 3D Mohr circle based on the stress map in *Qin et al., (2019)*, and a normalized parameter *understress* (equation 2) is used to quantify the criticality of the fault plane.

3.2.2 Results and Discussion
3.2.2.1 Focal mechanism results

We combine the polarities picking results from SVD method and machine learning method. We then select events with at least eight polarity picks, a maximum of station azimuth gap of 120º,

and a maximum of incident angle gap of 60º to invert for moment tensor. For Woodward and Fairview, due to the lack of station coverage, the azimuth gap cutoff is 100º to ensure quality. We get focal mechanisms for 305, 360, 464, and 631 events in Cushing, Guthrie, Woodward, and Fairview sequences, respectively. The real fault planes are differentiated from the auxiliary fault planes based on the main fault direction and regional stress field. The histograms of strike and dip angle of the selected fault planes are shown in Figure 6.

The strike orientations of individual fault planes are consistent with the inferred strike from seismicity. In Cushing sequence, the dominant strike is 225 -- 240º, and 69º of the fault planes are dipping steeply with a dipping angle larger than 70º. The Fairview sequence has a dominant strike of 210 – 225º, and 80% of the fault planes have a dipping angle larger than 70º. The dominant of the vertical fault planes are consistent with the vertical fault structures from seismicity. And the slight change of strikes in two clusters reflect the heterogeneity of the focal mechanisms in different regions of Oklahoma.

In Guthrie and Woodward, the majority of the fault planes have strike angle in the range of [30, 60]º and [210, 240]º. Although most of the events are dipping steeply, a small subset of the events have dip angles between 40 and 70º. The results are consistent with the observations from seismicity that the dipping angle changes with depth in Guthrie and Woodward.

We classify the faulting planes into different types by rake angle following *Chen et al., (2018)*. The spatial distribution of the focal mechanisms in each sequence is shown in Figure 6. To the first order of observation, Cushing and Fairview sequences show a dominate right-lateral strike-slip faulting on the main fault. In Cushing, the intersection point of the main fault and the secondary structures shows the occurrence of left-lateral strike-slip faults. In Fairview, the left-lateral strike-slip faults dominate the secondary structure. At shallow depth, a small fraction of normal events occurs in both sequences.

However, Guthrie and Woodward show a variety of faulting types on the main fault. In Guthrie, the main fault has a mix of strike-slip and normal slip components. The normal faulting events are mainly distributed beyond the extensional jog at depth of 6.5 km. In Woodward, the strike-slip events are at deeper depth and normal events at shallower depth, consistent with previous results *Qin et al., (2018)*. The newly ruptured segment has a dominant reverse slip component. It is strange that a large fraction of reverse faults occurs in a transtensional stress regime *(Qin et al., 2018)*. For those reverse events, we manually check the polarity picks and find no consistent error. One possible explanation is that during the active time of the sequence from 2016 to 2017, some temporary and industrial stations are available, while at the beginning and end of the sequence, a poor station coverage results in some inverted reverse components as an artifact. A cross-plot of the station azimuth gap and incident angle gap shows that most of the reverse events have poor station coverage with large azimuth gap and incident angle gap. We are further examining the data, and may exclude these reverse faulting events in the final analysis.
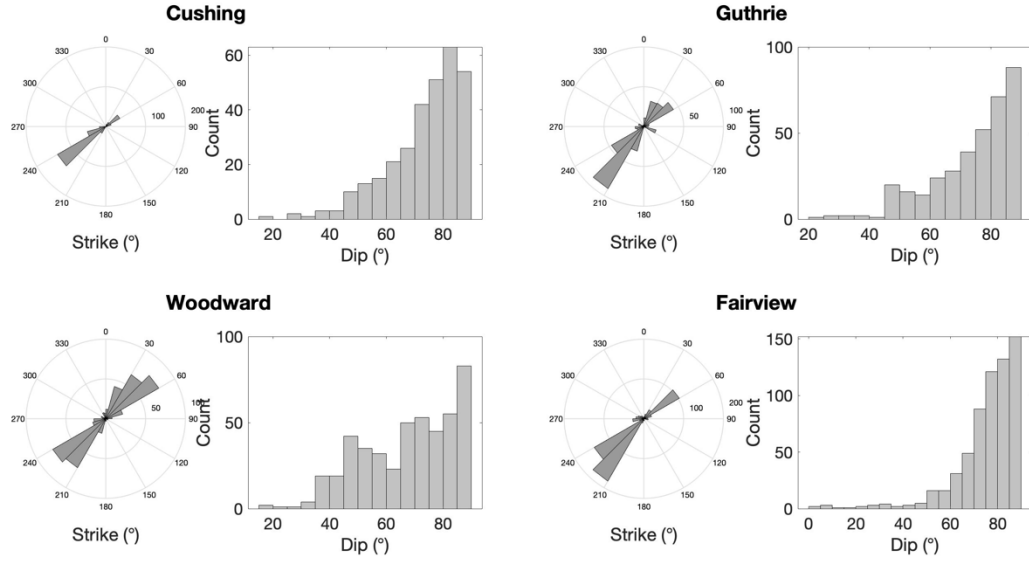
Figure 6. The histogram of strike and dip angles of focal mechanisms in four sequences. The plots include two fault planes from focal mechanism inversion.

3.2.2.2 Fault stress state evolutions

With the inverted focal mechanisms, we analyze the fault stress state in 3D Mohr circle. The regional stress field has been obtained by *Qin et al., (2019)*. The average principal stress amplitudes in Oklahoma are 30.0, 24.84, 15.46 MPa/km, respectively. And the σ_{Hmax} orientations in Cushing, Guthrie, Woodward, and Fairview are 86º, 79º, 85º, 78º, respectively. Following the previous method *Qin et al., (2019)*, we project the individual fault planes in each sequence onto 3D Mohr circle. The results are shown in Figure 7. We apply an *understress* cutoff of 0.2 to identify optimally oriented faults. For sequences with relatively clean focal mechanism solutions in Cushing and Fairview, the percentage of optimally oriented faults is the highest (82% and 80%). In Fairview, although the M5.1 main shock is not optimally oriented to the local stress field *(Qin et al., 2019)*, many small events are more critically stressed. This suggests that there may exist smaller fault fabrics that are more optimally oriented within the Fairview fault zone, which leads to prolonged foreshock sequences. Woodward has the lowest percentage due to the reverse slip components.

In Cushing, most of the events on the main fault are optimally oriented. The non-optimally oriented faults only occur on normal faulting events at shallow depth of the main fault and the intersection between the main fault and the secondary fault. In Fairview, the main fault is mostly optimally oriented with only the exception of some shallow events. Different from Cushing, many events on the secondary fault structure are also optimally oriented. In Guthrie, the main fault is less critically stressed than Cushing and Fairview due to the normal events. The main fault in Woodward is the least critically stressed of the four sequences. The strike-slip events are mostly optimally oriented, and the normal events at shallow depth are less optimally oriented. The rupture of the less optimally oriented normal events has been attributed to the earthquake interactions *(Qin et al., 2018)*. The newly rupture events at depth are the least optimally oriented.

Figure 8 show the temporal evolution of the four sequences. Cushing is featured by two mainshock-aftershock subsequences. The dominant faulting type is strike slip, and some normal

events occur after the M5.0 main shock. Each subsequence starts with large events that are optimally oriented (*understress*<0.2). In the following stage, some less optimally oriented events rupture, which are possibly triggered by earlier events. Guthrie is characterized as a swarm sequence without significantly large events. The sequence also starts with optimally oriented events, and the majority of the events have *understress* values between 0 and 0.5. Few non-optimally oriented events are triggered.
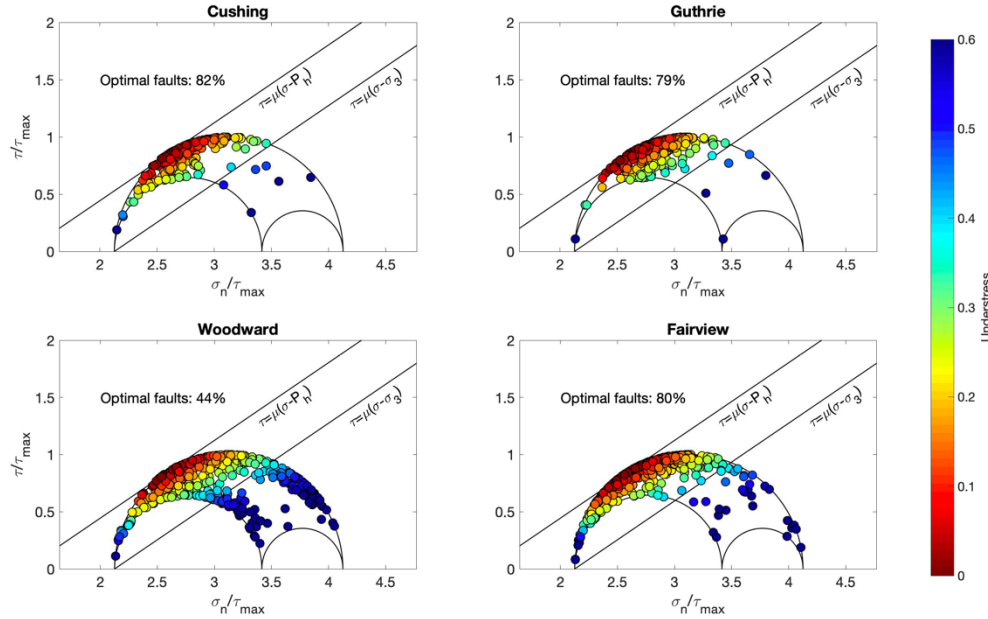

Figure 7. The stress state of individual fault planes in each sequence in 3D Mohr diagram. The three semi-circles represent the stress tensor, and the two straight lines represent the fault strength under hydrostatic fluid pressure and lithostatic pressure assuming a friction coefficient of 0.68.

The Woodward sequence is incomplete due to the poor station coverage at the beginning of the sequence. The events with large *understress* at the beginning and end of the sequence are possibly not well constrained due to station coverage. During the time from mid 2016 to 2018, when the temporary stations and industrial stations are available, we can still observe that the *understress* value increases with time in two subsequences from mid 2016 to 2017 and from 2017 to 2018, which suggests possibility of inter-event triggering with non-optimally oriented events.

The Fairview sequence peaked after Woodward, and most events in the sequence have higher quality focal mechanism solutions, highlighting the importance of station coverage. The sequence starts with optimally oriented events and triggers some non-optimally oriented events. Similar to Cushing, the mainshock leads an aftershock sequence. The two subsequences from 2016 to 2017 and from 2017 to 2018 show that the *understress* increases with time, which suggest the influences of earthquake interactions.

3.3 The early histories of seismicity in the Woodward and Fairview area

The focal mechanism analysis was focused on events from the OGS catalog. The Fairview/Woodward clusters began experiencing frequent small earthquakes in mid-2014, as documented in the Oklahoma Geological Survey (OGS) catalog *(Walter et al., 2020)*. However, at the time, seismic stations density was somewhat limited in the area and if we only use events listed in the current catalogs to study seismicity rate changes, we would not be able to understand the beginning and early evolution of seismicity in the area.

An effective way to identify possible "missing" events is the matched-filter technique. This technique utilizes waveforms or travel time information of known events as a template to search for similar patterns in the continuous recordings that would be suggestive of an event. It has been successfully applied to detect many unreported events that occurred at mid-ocean ridges and transform faults *(Ekström, 2006; Shearer, 1994)*, track low-frequency earthquakes within the deep tectonic tremor signals *(Shelly et al., 2007)*, detect early aftershocks *(Peng & Zhao, 2009)*, triggered earthquakes *(Meng et al., 2012)*, and foreshocks *(Walter et al., 2017)*.

We utilized the OGS earthquake catalog for traveltime information *(Walter et al., 2020)* and cut waveforms based on the cataloged pick times at analyst-picked phases. We bandpass filtered the templates between 4 and 10 Hz, cut the waveforms 1 s before and 10 s after the phase arrival (P or S), and resampled the data at a 20-Hz uniform sample rate. The matched-filter technique computes the normalized cross-correlation coefficient (coefficient between −1 and 1) at each sample point for each individual template through each component. Then, we shift each of the normalized cross-correlation functions produced for the individual components, relative to the travel time of each component and stack. Detection occurs when any point within the stacked cross-correlation function exceeds at least 9 times the median absolute deviation (MAD) of the daily stack. The MAD value of a detected event can be used to assess the relative quality of an event, whereby larger magnitude events that are clearly recorded by several stations would have a correspondingly higher MAD value.

Upon running the network-based matched-filter detection, we found that we were able to detect several earthquakes that had been missed by the routine catalog. Figure 9 includes detections for MAD>9 and MAD>12 for the Fairview and Woodward areas. We find that the Woodward cluster, which is the cluster to the west initiated first with robust seismicity in 2014 when examining those more robust detection thresholds (MAD>12). For relatively low MAD values, the detections suggest the possibility of even earlier activity on both the Woodward and Fairview faults, though some additional analysis would be required to further understand the robustness of those detections. In all cases, the detection capability of the matched-filter technique improved dramatically with the installation of additional rapid-response network stations in early 2016, as exhibited by the detection of negative magnitude events starting in early 2016 in Figure 9.
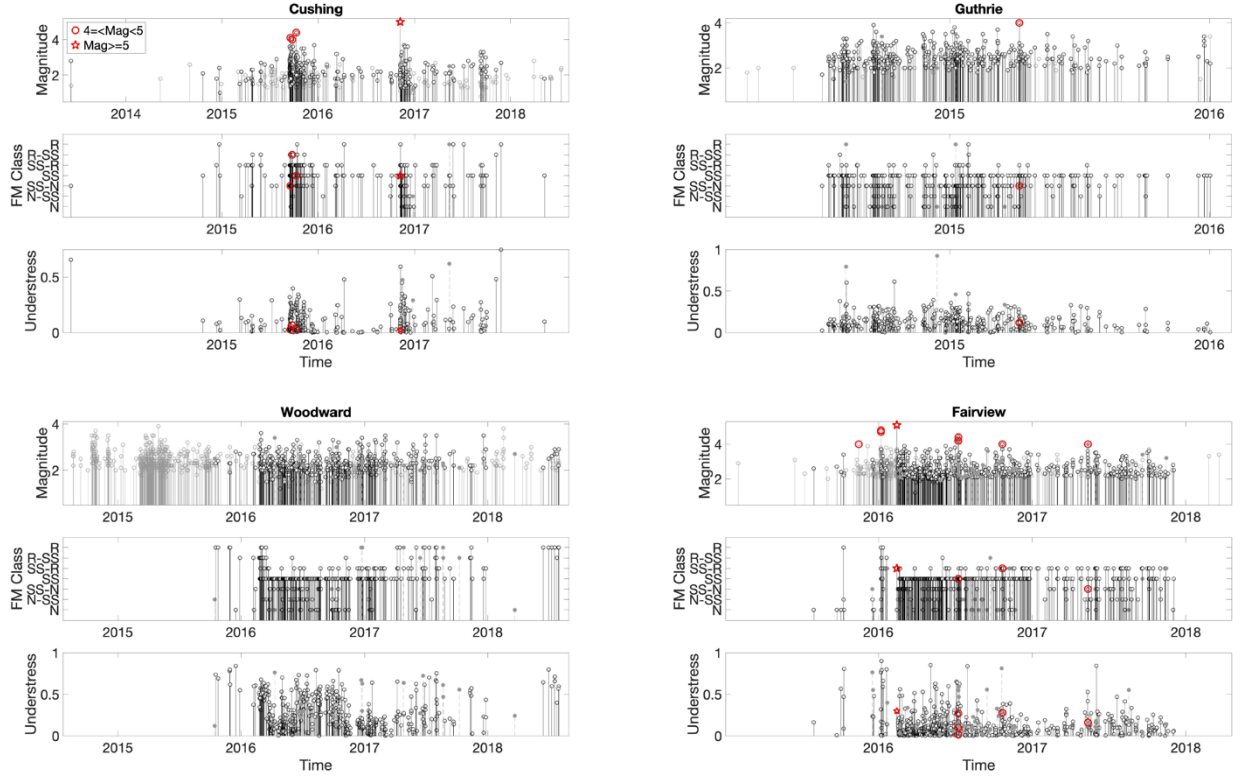
Figure 8. Temporal evolution of four sequences. The top panel shows the event magnitude with time (black and gray for events with and without inverted focal mechanisms). The middle panel shows the focal mechanism classes with time. The bottom panel shows the stress state of individual fault planes with time. The gray filled events are focal mechanisms of quality D. Star: M>=5 event; circles: M>=4.

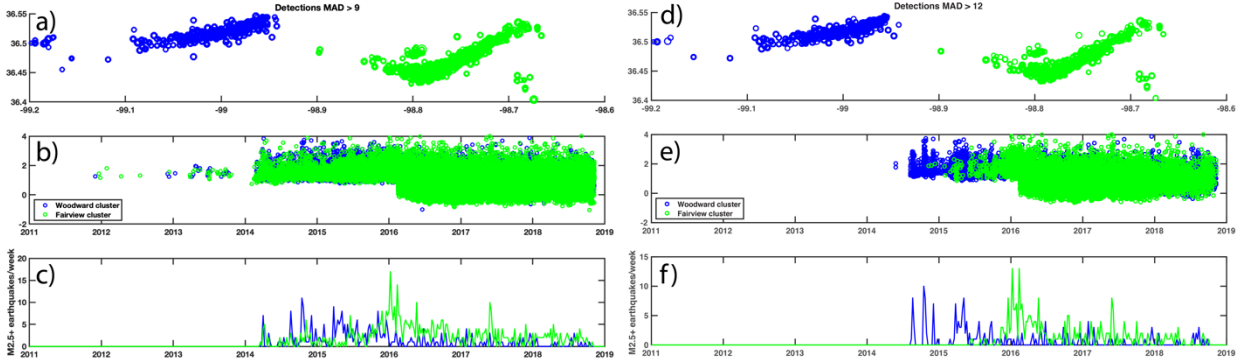*Figure 9. Network-based matched-filter detections for MAD > 9 (a-c) and MAD > 12 (d-f). Panels include the mapped location of the detected events, magnitude-time plots, and seismicity rate (events of M2.5 or greater per week).*

3.4 Summary

Analysis within individual sequences reveal considerable complexities compared to the overall stress state analysis from *Qin et al., (2019)*. The early stages of the Woodward and Fairview sequences are less reliably resolved due to limited station coverage in terms of stress state evolutions. Matched filter analysis suggests that the Woodward and Fairview sequences may become active before catalog, and the Fairview sequence may be activated at similar times with the Woodward sequence, however, the resolution may be limited due to station coverage at that time. For the Guthrie and Cushing sequences, we observe that both sequences started with

15

relatively more optimally oriented events. Less-optimally oriented events typically occur following larger earthquakes. This is similar to observations in the Prague sequence, where the largest aftershock occurred along a non-optimally oriented fault segment. The Fairview sequence is interesting, because the main fault is less optimally oriented compared to smaller events in the sequence, which suggests secondary fractures in the main fault zone were first triggered due to fluid injection. However, the M5 earthquake is controlled by pre-existing major geological structure. It would be interesting to further understand the inter-event triggering within the Fairview sequence to better understand the process leading to the mainshock.

3. Overall conclusion

In this project, we performed both large scale and small scale analysis of stress state variations. With large scale analysis, we find that most seismogenic faults are optimally oriented, however, some major sequences occurred along less-optimally oriented faults, such as the Fairview sequence in western Oklahoma. We also observe large scale correlation between modelled pore pressure and stress field, suggesting possible poroelastic influence of fluid injection on stress field.

With small scale analysis within individual faults, we find strong evidences for inter-event triggering and complex spatiotemporal stress evolutions. Even within a major fault zone that is less optimally oriented (such as the Fairview sequence), many smaller events occur along optimally oriented secondary faults. This indicates that pre-existing faults that are not optimally oriented for failure could be triggered and host a large earthquake. However, due to lack of good station coverage, the resolution of events prior to the M5 Fairview earthquake is not ideal, limiting further understanding of the pre-cursory processes. It is possible to use longer-term stations (that are in operation both before and after major earthquakes) to search for additional events that share highly-similar waveforms with cataloged earthquakes to further understand the temporal evolution of the sequence. However, detailed stress analysis may still be challenging.

Project Data:

The project did not generate new field observational data. The focal mechanism catalog used in the study is published as electronic supplemental material to the Qin et al., (2019). New focal mechanism solutions for smaller earthquakes are in preparation for publication and will be included as electronic supplemental materials to new publications. New template matching detected catalogs are being prepared for publication. Once both are published, we will send publications to USGS.

Acknowledgement of support:

Disclaimer:

The views and conclusions contained in this document are those of the authors and should not be interpreted as representing the opinions or policies of the U.S. Geological Survey. Mention of trade names or commercial products does not constitute their endorsement by the U.S. Geological Survey.

Bibliography:

Qin, Y., Chen, X., Walter, J. I., Haffener, J., Trugman, D. T., Carpenter, B. M., et al. (2019). Deciphering the stress state of seismogenic faults in Oklahoma and southern Kansas based on an improved stress map. Journal Geophysical Research: Solid Earth, 124. https://doi.org/10.1029/2019JB018377

Wu, Q., Chen, X., & Abercrombie, R. E. (2019). Source complexity of the 2015 Mw 4.0 Guthrie, Oklahoma earthquake. Geophysical Research Letters, 46. https://doi.org/10.1029/ 2019GL082690

References:

Alt, R. C., & Zoback, M. D. (2017). In Situ Stress and Active Faulting in Oklahoma. *Bulletin of the Seismological Society of America*, *107*(1), 1–13. https://doi.org/10.1785/0120160156

Chen, C. (2016). *Comprehensive analysis of Oklahoma earthquakes: from earthquake monitoring to 3D tomography and relocation*. University of Oklahoma.

Chen, X., Nakata, N., Pennington, C., Haffener, J., Chang, J. C., He, X., Zhan, Z., Ni, S., & Walter, J. I. (2017). The Pawnee earthquake as a result of the interplay among injection , faults and foreshocks. *Scientific Reports*, *7*(4945), 1–18. https://doi.org/10.1038/s41598-017-04992-z

Ekström, G. (2006). Global detection and location of seismic sources by using surface waves. *Bulletin of the Seismological Society of America*, *96*(4 A), 1201–1212. https://doi.org/10.1785/0120050175

Gischig, V. S. (2015). Rupture propagation behavior and the largest possible earthquake induced by fluid injection into deep reservoirs. *Geophysical Research Letters*, *42*(18), 7420–7428. https://doi.org/10.1002/2015GL065072

Goebel, T., Weingarten, M., Chen, X., Haffener, J., & Brodsky, E. E. (2017). The 2016 Mw5.1 Fairview, Oklahoma earthquakes: Evidence for long-range poroelastic triggering at 40 km from fluid disposal wells. *Earth and Planetary Science Letters*, *472*, 50–61. https://doi.org/10.1016/j.epsl.2017.05.011

Haffener, J., Chen, X., & Murray, K. (2018). Multiscale Analysis of Spatiotemporal Relationship Between Injection and Seismicity in Oklahoma. *Journal of Geophysical Research: Solid Earth*, *123*(10), 8711–8731. https://doi.org/10.1029/2018JB015512

Hardebeck, J. L., & Michael, A. (2006). Damped regional-scale stress inversions: methodology and examples for southern California and the Coalinga aftershock sequence. *J. Geophys. Res.*, *111*(B11310). https://doi.org/10.1029/2005JB004144

Hardebeck, J. L., & Shearer, P. M. (2003). Using S/P amplitude ratios to constrain the focal mechanisms of small earthquakes. *Bulletin of the Seismological Society of America*, *93*(6), 2434–2444. Retrieved from %7B%3C%7DGo

Keranen, K. M., Weingarten, M., Abers, G. A., Bekins, B. A., & Ge, S. (2014). Sharp increase in central Oklahoma seismicity since 2008 induced by massive wastewater injection. *Science*. https://doi.org/10.1126/science.1255802

Kwiatek, G., Martínez-Garzón, P., & Bohnhoff, M. (2016). HybridMT: A MATLAB/Shell Environment Package for Seismic Moment Tensor Inversion and Refinement. *Seismological Research Letters*, *87*(4), 964–976. https://doi.org/10.1785/0220150251

Langenbruch, C., Weingarten, M., & Zoback, M. D. (2018). Physics-based forecasting of man-made earthquake hazards in Oklahoma and Kansas. *Nature Communications*, *9*(1), 1–10. https://doi.org/10.1038/s41467-018-06167-4

Lund Snee, J., & Zoback, M. D. (2016). State of stress in Texas: Implications for induced seismicity. *Geophysical Research Letters*, *43*, 208–214. https://doi.org/10.1002/2016GL070974

Martínez-garzón, P., Kwiatek, G., Ickrath, M., & Bohnhoff, M. (2014). MSATSI: A MATLAB Package for Stress Inversion Combining Solid Classic Methodology, a New Simplified User-Handling, and a Visualization Tool, (August). https://doi.org/10.1785/0220130189

Martínez-Garzón, P., Bohnhoff, M., Kwiatek, G., & Dresen, G. (2013). Stress tensor changes related to fluid injection at the Geysers geothermal field, California. *Geophysical Research Letters*, *40*(11), 2596–2601. https://doi.org/10.1002/grl.50438

Meng, X., Yu, X., Peng, Z., & Hong, B. (2012). Detecting Earthquakes around Salton Sea Following the 2010 Mw7.2 El Mayor-Cucapah Earthquake Using GPU Parallel Computing . *Procedia Computer Science*, *9*, 937–946. https://doi.org/doi: 10.1016/j.procs.2012.04.100

Michael, A. J. (1984). Determination of stress from slip data: faults and folds. *Journal of Geophysical Research*, *89*(B13), 11517–11526. https://doi.org/10.1029/JB089iB13p11517

Peng, Z., & Zhao, P. (2009). Migration of early aftershocks following the 2004 Parkfield earthquake. *Nature*, *2*. https://doi.org/DOI: 10.1038/NGEO697

Qin, Y., Chen, X., Carpenter, B. M., & Kolawole, F. (2018). Coulomb Stress Transfer Influences Fault Reactivation in Areas of Wastewater Injection. *Geophysical Research Letters*, (Figure 1), 1–9. https://doi.org/10.1029/2018GL079713

Quinones, L. A., DeShon, H. R., Magnani, M. B., & Frohlich, C. (2018). Stress orientations in the fort worth basin, texas, determined from earthquake focal mechanisms. *Bulletin of the Seismological Society of America*, *108*(3), 1124–1132. https://doi.org/10.1785/0120170337

Ross, Z. E., Meier, M. A., & Hauksson, E. (2018). P Wave Arrival Picking and First-Motion Polarity Determination With Deep Learning. *Journal of Geophysical Research: Solid Earth*, *123*(6), 5120–5129. https://doi.org/10.1029/2017JB015251

Rubinstein, J. L., Ellsworth, W. L., & Dougherty, S. L. (2018). The 2013–2016 induced earthquakes in harper and sumner counties, Southern Kansas. *Bulletin of the Seismological Society of America*, *108*(2), 674–689. https://doi.org/10.1785/0120170209

Schoenball, M., & Ellsworth, W. L. (2017). Waveform-Relocated Earthquake Catalog for Oklahoma and Southern Kansas Illuminates the Regional Fault Network. *Seismological Research Letters*, *88*(5), 1252–1258. https://doi.org/10.1785/0220170083

Shearer, P. (1994). Global seismic event detection using a matched filter on long-period seismograms. *J. Geophys. Res.*, *99*(B7), 13713–13725.

Shelly, D R, Beroza, G. C., & Ide, S. (2007). Non-volcanic tremor and low-frequency earthquake swarms. *Nature*, *446*(7133), 305–307. https://doi.org/10.1038/nature05666

Shelly, David R., Hardebeck, J. L., Ellsworth, W. L., & Hill, D. P. (2016). A new strategy for earthquake focal mechanisms using waveform-correlation-derived relative polarities and cluster analysis: Application to the 2014 Long Valley Caldera earthquake swarm. *Journal of Geophysical Research: Solid Earth*, *121*(12), 8622–8641. https://doi.org/10.1002/2016JB013437

Terakawa, T., Zoporowski, A., Galvan, B., & Miller, S. A. (2010). High-pressure fluid at hypocentral depths in the L'Aquila region inferred from earthquake focal mechanisms. *Geology*, *38*(11), 995–998. https://doi.org/10.1130/g31457.1

Vidale, J. E., & Shearer, P. M. (2006). A survey of 71 earthquake bursts across southern California: Exploring the role of pore fluid pressure fluctuations and aseismic slip as drivers. *Journal of Geophysical Research-Solid Earth*, *111*(B5). https://doi.org/B05312 10.1029/2005jb004034

Walter, J. I., Chang, J. C., & Dotray, P. J. (2017). Foreshock Seismicity Suggests Gradual Differential Stress Increase in the Months Prior to the 3 September 2016 M w 5 . 8 Pawnee Earthquake. *Seismol. Res. Lett.*, *88*(4), 4–11. https://doi.org/10.1785/0220170007

Walter, J. I., Ogwari, P., Thiel, A., Ferrer, F., Woelfel, I., Chang, J. C., Darold, A. P., & Holland, A. A. (2020). The Oklahoma Geological Survey Statewide Seismic Network. *Seismological Research Letters*, *91*(2A), 611–621. https://doi.org/10.1785/0220190211

Wu, Q., Chapman, M. C., & Chen, X. (2018). Stress Drop Variations of Induced Earthquakes in Oklahoma. *Bulletin of the Seismological Society of America*, *108*(3A), 1107–1123. https://doi.org/10.1785/0120170335

Ye, L., Kanamori, H., & Lay, T. (2018). Global variations of large megathrust earthquake rupture characteristics. *Science Advances*, *4*(3), 1–8. https://doi.org/10.1126/sciadv.aao4915

Yeck, W. L., Hayes, G. P., McNamara, D. E., Rubinstein, J. L., Barnhart, W. D., Earle, P. S., & Benz, H. M. (2016). Oklahoma experiences largest earthquake during ongoing regional wastewater injection hazard mitigation efforts. *Geophysical Research Letters*, *44*(September 2016), 711–717. https://doi.org/10.1002/2016GL071685

Yoshida, K., Hasegawa, A., & Yoshida, T. (2016). Temporal variation of frictional strength in an earthquake swarm in NE Japan caused by fluid migration. *Journal of Geophysical Research: Solid Earth*, *121*(8), 5953–5965. https://doi.org/10.1002/2016JB013022

Yoshida, K., Saito, T., Urata, Y., Asano, Y., & Hasegawa, A. (2017). Temporal Changes in Stress Drop, Frictional Strength, and Earthquake Size Distribution in the 2011 Yamagata-Fukushima, NE Japan, Earthquake Swarm, Caused by Fluid Migration. *Journal of Geophysical Research: Solid Earth*, *122*(12), 10,379-10,397. https://doi.org/10.1002/2017JB014334

Zhang, Q., & Shearer, P. M. (2016). A new method to identify earthquake swarms applied to seismicity near the San Jacinto Fault, California. *Geophysical Journal International*, *205*(2), 995–1005. https://doi.org/10.1093/gji/ggw073